RESEARCH ARTICLE

WILEY

Brain signatures based on structural MRI: Classification for MCI, PMCI, and AD

Venkateswarlu Gonuguntla[1] 🔟 | Ehwa Yang[1] | Yi Guan[2] | Bang-Bon Koo[2] | Jae-Hun Kim[3]

[1]Medical Science Research Institute, Samsung Medical Center, Seoul, South Korea

[2]Department of Anatomy and Neurobiology, Boston University School of Medicine, Boston, Massachusetts, USA

[3]Department of Radiology, Samsung Medical Center, Sungkyunkwan University School of Medicine, Seoul, South Korea

Correspondence
Jae-Hun Kim, Department of Radiology, Samsung Medical Center, Sungkyunkwan University School of Medicine, Seoul, South Korea.
Email: jaehun.kim78@gmail.com

Abstract

Structural MRI (sMRI) provides valuable information for understanding neurodegenerative illnesses such as Alzheimer's Disease (AD) since it detects the brain's cerebral atrophy. The development of brain networks utilizing single imaging data—sMRI is an understudied area that has the potential to provide a network neuroscientific viewpoint on the brain. In this paper, we proposed a framework for constructing a brain network utilizing sMRI data, followed by the extraction of signature networks and important regions of interest (ROIs). To construct a brain network using sMRI, nodes are defined as regions described by the brain atlas, and edge weights are determined using a distance measure called the Sorensen distance between probability distributions of gray matter tissue probability maps. The brain signatures identified are based on the changes in the networks of disease and control subjects. To validate the proposed methodology, we first identified the brain signatures and critical ROIs associated with mild cognitive impairment (MCI), progressive MCI (PMCI), and Alzheimer's disease (AD) with 60 reference subjects (15 each of control, MCI, PMCI, and AD). Then, 200 examination subjects (50 each of control, MCI, PMCI, and AD) were selected to evaluate the identified signature patterns. Results demonstrate that the proposed framework is capable of extracting brain signatures and has a number of potential applications in the disciplines of brain mapping, brain communication, and brain network-based applications.

KEYWORDS
Alzheimer's disease (AD), brain signatures, gray matter, structural MRI (sMRI), tissue probability maps

1 | INTRODUCTION

Structural MRI (sMRI) is a non-invasive clinical imaging technique that is frequently used to examine the anatomy and disease of the brain (Frisoni et al., 2010; Vemuri & Jack, 2010). Recently, researchers have concentrated on the network modifications associated with neurodegenerative illnesses such as Alzheimer's Disease (AD). It is a subjective

disease that typically begins with moderate cognitive impairment (MCI). Individual network modifications may enable the identification of people who progress from MCI to AD, and an understanding of these changes throughout the transition may aid in delaying the conversion from MCI to AD. Several studies over the last decade have identified some underlying brain network patterns associated with disease using one or more neuroimaging modalities such as diffusion

magnetic resonance imaging (dMRI), functional magnetic resonance imaging (fMRI), structural magnetic resonance imaging (sMRI), electro-encephalography (EEG), and positron emission tomography (PET) (Apostolova & Thompson, 2007; Brier et al., 2014; Dai et al., 2019; Filippi & Agosta, 2011; Filippi et al., 2020; Hojjati et al., 2018; Li et al., 2019). The majority of currently available strategies for finding disease-related brain networks combine data from numerous participants to generate a single network. This limits our ability to comprehend an individual subject and the network changes in their brain anatomy. Additionally, the construction of a network matrix for an individual is a difficult task due to other limitations associated with the use of each modality (e.g., building a network matrix based on correlation methods is more efficient when using EEG and fMRI data, but is inefficient when using sMRI and PET data, which have only one time point (Jiang et al., 2017). Also, comparing different brain regions within an individual using sMRI requires an adequate mapping of voxels to regions.

To address these concerns, works such as (Beheshti et al., 2017; Tijms et al., 2012) divided the brain into uniform cubes and defined a network as the correlations between the cubes. As a result, it is difficult to map the functional areas of the brain. In order to get around this problem, (Kong et al., 2015) devised a method for identifying individual brain networks, and then the metrics of those networks could be used to look at the individual variances of more complex network structures. In this investigation, the Kullback-Leibler (KL) divergence method was used to generate the entire network matrix, and the binary network was constructed using various threshold levels, which has the limitation of mapping an individual to the best network connections. A method based on principal component analysis (PCA) and mutual information (MI) was suggested in (Jiang et al., 2017). PCA was used to extract the deeper features at each node, and MI of principal components (PCs) was used to determine the weight of the edges between each pair of nodes. The importance of PCs was not evident in this research, and more importantly, PCA analysis can only be performed on numerous participants.

To overcome the complexity limitations of the KL method as described in (Kong et al., 2015) and the use of multiple subjects to find PCs as described in (Jiang et al., 2017), we propose to use the Sorensen similarity measure between probability distributions of gray matter tissue probability maps (TPMs) to construct an individual brain network. The construction of a unique brain network in relation to the sMRI enables direct interpretation of the regions and their similarities/dissimilarities. The proposed approach is less complex and allows to form ROI-based structural connectivity from an individual sMRI. Also, it prepares the groundwork for a study focused on a single subject. Further, identifying condition-related brain signatures from these brain networks may provide a neuroscientific network perspective on brain analysis, as brain signatures may easily distinguish between conditions and provide a deeper knowledge of the brain.

In this work, we provided a methodology for constructing an individual brain network only based on sMRI data, followed by the identification of brain signatures based on sMRI-related brain networks. The brain networks are constructed utilizing the gray matter TPMs of

60 subjects (15 each of control, MCI, progressive MCI (PMCI), and AD) sMRI, employing atlas-based regions as nodes and the Sorensen distance measure between probability distributions of regions as edges. The brain signature of each condition is then identified by comparing the disorder's networks to those of normal subjects (in this paper, term condition refers to MCI, PMCI, or AD). Additionally, significant ROIs associated with each condition are found. Finally, 200 examination subjects were used to investigate the identified brain signatures (50 each of control, MCI, PMCI, and AD).

This paper is structured as follows. Section 2 discusses the data preparation process, the methodologies for finding brain signatures, and the critical ROIs of related sMRI. Section 3 summarizes the findings, while Section 4 discusses and concludes the work with recommendations for future work.

2 | MATERIALS AND METHODS

The objectives of this study are to create an individual brain network using sMRI data and to discover brain signatures and important ROIs associated with any condition using the formulated brain networks. The proposed framework for extracting brain signatures is summarized in Figure 1. As shown in Figure 1, stage A involves the use of Freesurfer (FreeSurfer, 2012) to extract the brain from an MRI and then is transformed to MNI standard space (MNI152 T1 1mm brain) (Collins et al., 1995; Mazziotta et al., 2001). The MR images were then segmented and smoothed to reveal gray matter TPMs. In step B, regions based on the human brain atlas were employed to deduce the connection matrix/brain network from gray matter TPMs. Stage C describes a threshold selection approach for extracting brain signatures. Stage D describes the detection of brain signatures, ROIs, and the merging/fusion of brain signatures into a single network for usage in applications. Finally, in stage E, the detected brain signatures are used to categorize examination subjects as part of the framework's evaluation. The following subsections A-E discuss the methodologies for identifying brain signatures and their application.

2.1 | Participants

Data used in the preparation of this article were obtained from the Alzheimer's Disease Neuroimaging Initiative (ADNI) database (adni. loni.usc.edu). The ADNI was launched in 2003 as a public-private partnership, led by Principal Investigator Michael W. Weiner, MD. The primary goal of ADNI has been to test whether serial magnetic resonance imaging (MRI), positron emission tomography (PET), other biological markers, and clinical and neuropsychological assessment can be combined to measure the progression of mild cognitive impairment (MCI) and early Alzheimer's disease (AD).

A total of 260 subjects were employed in this investigation, and the subjects included in this study are listed in Table 1. The ADNI Subject IDs and Image Data IDs for the reference subjects (60) and examination subjects (200) indicated in Table 1 are available online at
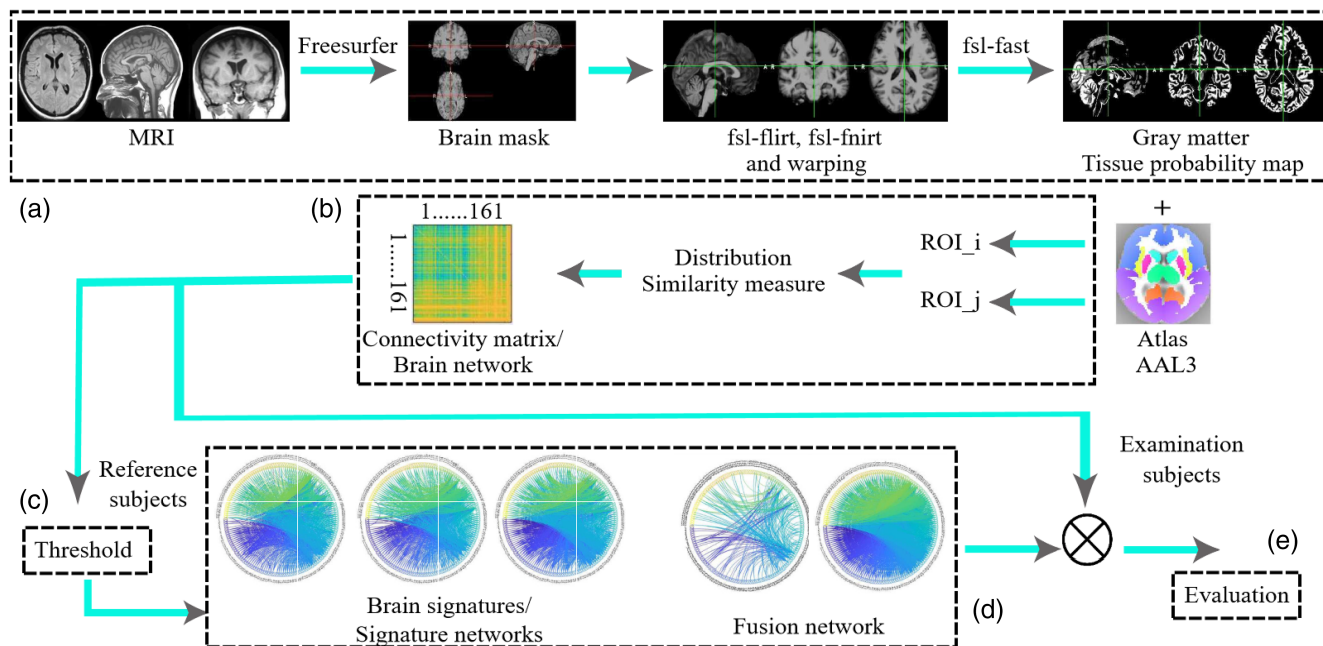
FIGURE 1 Identification of brain signature networks from sMRI—workflow diagram

TABLE 1 Subjects considered in this study

Group	Control	MCI	PMCI	AD
Reference subjects (60)	15	15	15	15
Examination subjects (200)	50	50	50	50

https://surfer.nmr.mgh.harvard.edu/fswiki/AdnidevtestV6 and https://github.com/christiansalvatore/Salvatore-200Longitudinal, respectively. The inclusion criteria are as described in (Salvatore et al., 2018). The criteria for control subjects are: Mini Mental State Examination (MMSE) scores between 24 and 30; Clinical Dementia Rating (CDR) of zero; absence of depression, MCI, and dementia. For MCI, patients had to have an MMSE score of 24-30 on the CDR, no other cognitive symptoms of impairment, and no signs of dementia. For AD, MMSE scores of 20 to 26; a CDR of 0.5 or 1.0; and the criteria for the probable AD are as per Alzheimer's Disease and Related Disorders Association's.

2.2 | MRI and gray matter tissue probability maps

For the analysis purpose, among the subjects described in Table 1, all examination subjects used sMRI images of the stable diagnosis (time-zero point) as specified in (Salvatore et al., 2018), while reference subjects utilized images at all accessible time points. All images were obtained at 1.5 T using a T1-weighted sequence in accordance with the ADNI standard. All MR images were corrected for 3D gradwarp and B1 non-uniformity. Following that, brain extraction from sMRI images was performed using Freesurfer. The extracted brain is then transformed into a standard Montreal Neurological Institute (MNI)

space using the fsl-flirt, fsl-fnirt, and warping procedures (FSL is a tool for analyzing fMRI, MRI, and DTI brain imaging data; see (Jenkinson et al., 2012; Smith et al., 2004; Woolrich et al., 2009). Finally, using fsl-fast segmentation, the transformed extracted brain was segmented into gray matter TPM. The following section describes how an individual brain network is constructed using gray matter TPM.

2.3 | Brain network from individual sMRI

The brain network's construction is critical for the network-based analysis of the brain. The constructed brain networks can be used in any application that makes use of brain networks (Bullmore & Sporns, 2009; Rubinov & Sporns, 2010; Sporns, 2013). To convert the gray matter TPM from sMRI to a brain network, the nodes and edges must be properly defined. In this work, nodes indicate brain regions, and edges reflect the distance between nodes in terms of the distribution of gray matter TPMs. To begin, we utilized 161 (75 for each hemisphere and Vermis 1 2, Vermis 3, Vermis 4 5, Vermis 6, Vermis 7, Vermis 8, Vermis 9, Vermis 10, VTA, LC, Raphe) cortical and subcortical ROIs from the widely used automated anatomical labeling atlas 3 (AAL3) as nodes (Rolls et al., 2020).

To define the edges between brain regions, several distance/similarity measures available in the literature (Cha, 2007; Pastore & Calcagni, 2019) were used and identified the edges between brain regions (Beheshti et al., 2017; Jiang et al., 2017; Kong et al., 2015; Tijms et al., 2012). In this study, we identify the edges between the distributions of gray matter TPM in ROIs using the Sorensen distance dissimilarity measure (Sorensen, 1948). Sorensen distance dissimilarity is based on the absolute difference between distributions and is a widely used measure of dissimilarity because it is less complex, retains

sensitivity in more heterogeneous data, and gives less weight to out-liers (McCune et al., 2002). Between two distributions p and q, the Sorensen distance dissimilarity measure d_{sor} is defined as follows:

$$d_{sor} = \frac{\sum_{i=1}^{N} |p_i - q_i|}{\sum_{i=1}^{N} (p_i + q_i)} \qquad (1)$$

where p and q denote two probability distributions. d_{sor} is in the range of [0 1], where 0 indicates identical distributions—denotes no dissimilarity, and 1 indicates the highest dissimilarity. The distribution of each ROI is determined for each subject using kernel density estimation from gray matter TPM. Then, the d_{sor} values of all pairs of brain regions result in a 161 × 161 matrix that is referred to as the brain network. The matrix of dimension 161 × 161 of each subject is referred to as the subject's Sorensen matrix (SM). Extraction of significant patterns or brain signatures from the brain network enables us to represent any condition or task-related sMRI using a network connection, providing new insights into the brain. To accomplish this, it is necessary to examine the right selection of the threshold. The following section discusses how to choose a threshold for extracting brain signatures.

2.4 | Network threshold

The topic of network threshold selection remains unsolved in neuro-science. We previously developed strategies for determining the threshold based on the network's efficiency and energy consumption (Gonuguntla et al., 2020; Gonuguntla & Kim, 2020). In general, these strategies are applicable to any modality. To determine the threshold, the following approach is used as described in (Gonuguntla & Kim, 2020). To begin, a differential brain network (DBN) is identified using the following equation based on the dissimilarities between the condition and the control subject:

$$\text{DBN}_{\text{disease}} = <\text{SM}^{\text{disease}}> - <\text{SE}^{\text{control}}> \qquad (2)$$

where $<\text{SM}^{\text{disease}}>$ is the element-wise mean of the SMs of the disease subject and $<\text{SM}^{\text{control}}>$ is the element-wise mean of the SMs of the control subject. $\text{DBN}_{\text{disease}}$ for MCI, PMCI, and AD can all be performed using (2). Because the $\text{DBN}_{\text{disease}}$ is based on the relative change with control subjects, it gives information about the condition's direct variations when compared to control participants. As a result, $\text{DBN}_{\text{disease}}$ is chosen for analysis. Then, the top few edges with the highest changes were chosen to represent the condition and its associated brain network. To identify these edges with the highest differences, the following disease-related network threshold (DRNT) selection procedure is used:

1. arrange all $\text{DBN}_{\text{disease}}$ values in descending order (the arranged values represent the edges of the network)

2. formulate the network with M selected edges (M indicates the top M edges that were arranged in descending order)

3. for M = 1 to $_n C2$, evaluate the global cost-efficiency (GCE)

$$\text{GCE} = \text{GE} - \text{cost} \qquad (3)$$

where, GE is the global efficiency (the average inverse shortest path length in the network (Bullmore & Sporns, 2009; Dimitriadis et al., 2017; Rubinov & Sporns, 2010) and the cost is the ratio of the total weight of the selected network edges to the total weight of the fully connected network edges. For instance, if the network is formulated using top 'M' edges then, GE can be computed as

$$\text{GE} = \frac{1}{n(n-1)} \sum_{i \neq j \in G} \frac{1}{d_{ij}}$$

and *cost* as

$$\text{cost} = \frac{e_S}{e_T}$$

where d_{ij} is the shortest path length between nodes i and j in the network (G), n is the total number of nodes in the network, e_S is the total weight of the selected network edges, and e_T is the total weight of the fully connected network edges. Thus, GCE for every "M" can be computed using (3).

4. finally, identify "M" corresponds to the maximum value in (3)

The DRNT of MCI, PMCI, and AD can be identified using the procedure outlined above. The network threshold is defined in each condition as the number of pairs that result in optimal GCE. The next sections explain the extraction of brain signatures and their fusion network for usage in applications.

2.5 | Brain signatures and important ROIs

The optimal number of pairs selected via GCE results in the formation of a brain signature, which is referred to as the representation of the condition-related sMRI with its signature network. These networks serve as the foundation for understanding the brain in terms of networks and can be applied to any network-based application. The signature networks are analyzed to identify the top few nodes with the highest degree as significant ROIs. All of the detected signature networks can be combined to produce a single network for use in classification applications. To demonstrate, the fusion network of the identified brain signatures is constructed as a (a) common network—a network composed of common edges that appeared in all conditions—and a (b) full network—a network composed of all edges that appear in all conditions. These fusion networks could serve as the foundation for a variety of applications involving brain networks. The examination of the resulting common network could provide a

backbone structure for the condition, and the entire network could be used for classification purposes. The following part demonstrates the use of the identified brain signature by classifying examination patients into control, MCI, PMCI, and AD groups using the fusion network's Sorensen distance dissimilarity measures as features.

2.6 | Application

In this study, we demonstrate the application of brain signature networks by classifying 200 examination subjects into control, MCI, PMCI, and AD. The classification results with fusion network as features at stable diagnosis are achieved using support vector machines (SVMs) as classifiers with a one-against-one strategy.

3 | RESULTS

The brain networks of each subject's sMRI provided in Table 1 were identified using the proposed framework for identifying the individual brain network associated with sMRI. The identification of brain signatures and fusion networks is carried out using the methods outlined in Sections 2.3 and 2.4 (only 60 reference subjects were used to identify the brain signatures and fusion networks). Finally, the 200 examination subjects are classified using the identified brain signatures as a demonstration of the suggested approach. In the illustrations of the brain network maps and brain signatures, nodes 1–75 correspond to the left hemisphere, nodes 87–161 (arranged in reverse order to maintain symmetry with the left hemisphere) to the right hemisphere, and nodes 76–86 correspond to Vermis 1 2, Vermis 3, Vermis 4 5, Vermis 6, Vermis 7, Vermis 8, Vermis 9, Vermis 10, VTA, LC, Raphe. Additionally, the appendix contains anatomical descriptions and labeling for all ROIs analyzed of the subjects presented in Table 4. The next

section illustrates the outcomes produced by employing the provided methods.

3.1 | MRI and gray matter tissue probability maps

The gray matter TPMs of all subjects were detected using the procedure outlined in Section 2.1. To begin, the brain was extracted using freesurfer and then translated to MNI space using fsl non-linear registration. Then, using fsl-fast segmentation, these transformed images were segmented into gray matter TPMs. During the fsl main segmentation phase, the MRF beta value was set to 0.5 to provide spatial smoothing and the bias field was smoothed using a 10mm full-width at half-maximum (FWHM). To illustrate the gray matter TPMs directly, a representative gray matter TPM from a randomly selected sMRI is shown in Figure 2. These gray matter TPMs have been extensively employed in group studies of brain structure and network analysis (Koikkalainen et al., 2016; Li et al., 2011; Rimkus et al., 2019). Given that the current study is focusing on the construction of an individual brain network associated with sMRI, the following section details the conceptual transformation of these TPMs into brain networks.

3.2 | Brain network from individual sMRI

To form a brain network that corresponds to sMRI, the nodes and edges of each gray matter TPM are specified as outlined in Section 2.2. Using all reference subjects and at each voxel location, we tested for the null hypothesis that the TPMs come from a distribution with a mean of 0. If the lower limit of the confidence interval (CI) is less than or equal to 0, the voxel location is considered insignificant and is removed from the analysis. The remaining voxel values were then used to identify 161 ROIs, dubbed nodes, based on the AAL3 brain
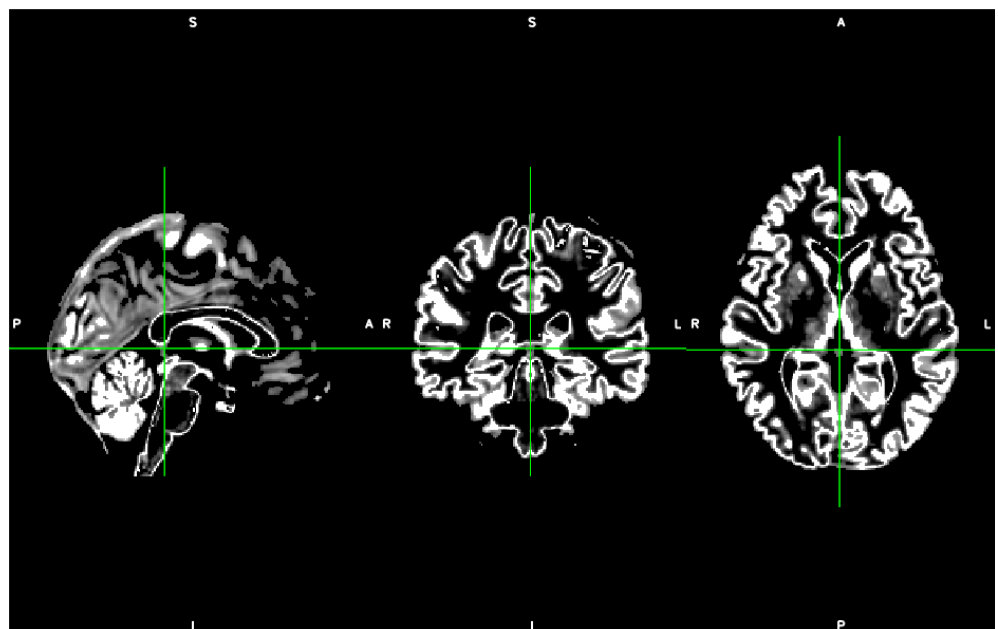

FIGURE 2 Gray matter tissue probability map illustration. The brighter the color, the greater the probability that the voxel is gray matter, while the darker the color, the lesser the probability that the voxel is gray matter

atlas. For ROI, the distribution is calculated using the gray matter's TPM (161 ROIs in total). Finally, an SM of size 161×161 is formed for each subject using (1) and is referred to as the brain network associated with sMRI.

The differences in the brain networks of each disease when compared to controls serve as the foundation for the development of brain signatures. To illustrate the differences between each condition and control subjects, Figure 3 shows the average maps of the brain networks and the dissimilarities identified by employing (2) for all conditions. Additionally, the difference values for each condition are shown in Figure 3 (bottom panel) as histogram function. To visualize the difference values in each condition, Figure 4 shows some selected pairings illustrating the positive and negative differences of one subject per each condition. The subplots in rows correspond to subjects with control, MCI, PMCI, and AD (from top to bottom). Each pair's Sorensen distance dissimilarity is also shown in the figure at the top of each subplot. The yellow shaded regions indicate that the selected pairs have a lower similarity score when compared to the control subject, and vice versa for the cyan blue colored pairs. The same phenomenon was found across multiple pairs and subjects. Only selected pairs of one subject per condition are given for demonstration purposes. These distinctions serve as the foundation for forming the brain signatures associated with any condition.

To aid in visualizing the differences between MCI, PMCI, and AD subjects when compared to controls, the kernel density estimation of all the differences for all conditions is provided in Figure 5. From Figure 3 (bottom panel) and Figure 5, in comparison to control

participants, we can identify various positive and negative differences in MCI, PMCI, and AD. Also, these differences are greatest in AD and are smallest in MCI. These variances are attributed to the dissimilarities in the distributions of the respective regions, which demonstrates the structural disturbances in diseased people when compared to normal subjects. Thus, it enables us to identify the regions corresponding to structural disruptions in the diseased subject (e.g., visually identified regions are generally similar to those identified by previous brain network studies (Bassett et al., 2008; Chen et al., 2008; Gong et al., 2009; He et al., 2007; Khundrakpam et al., 2013; Sanz-Arigita et al., 2010; Spulber et al., 2013) and their analysis in detail was carried out in the subsequent sections). Additionally, the extraction of significant patterns/signature networks and their network analysis enables us to depict the condition using a network connection, which provides new insights into the brain's associated conditions. The following section discusses how the threshold for identifying brain signatures was determined and how it was analyzed.

3.3 | Network threshold

To set the threshold, all the $DBN_{disease}$ values for each condition are identified using (2) and are orderly arranged. The large differences present in each condition are a result of the structural disruptions prevalent in that condition when compared to normal subjects. Thus, by expressing brain signatures using these connections, we can gain a better understanding of the relevant condition. To most accurately
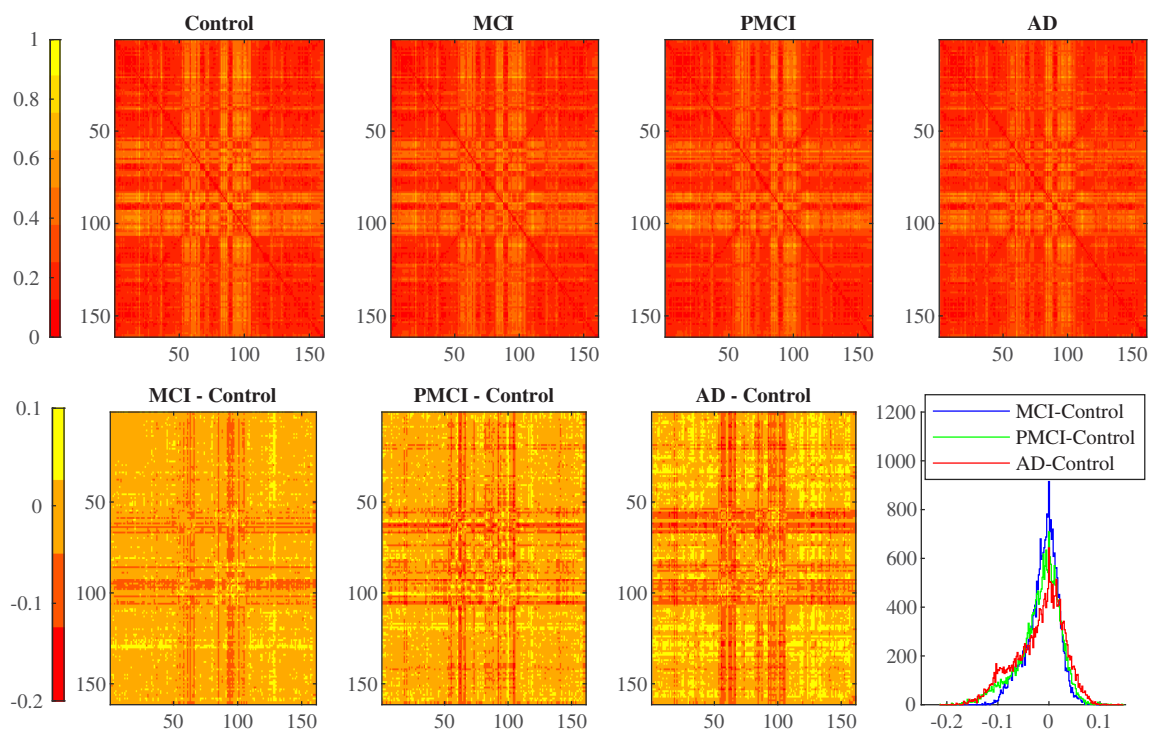

FIGURE 3 The average brain networks in each condition (top) and the differences in dissimilarities between regions in each condition when compared to control subjects (bottom). The dissimilarities identified with (2) as a histogram for all conditions are depicted in the bottom panel's final sub-figure
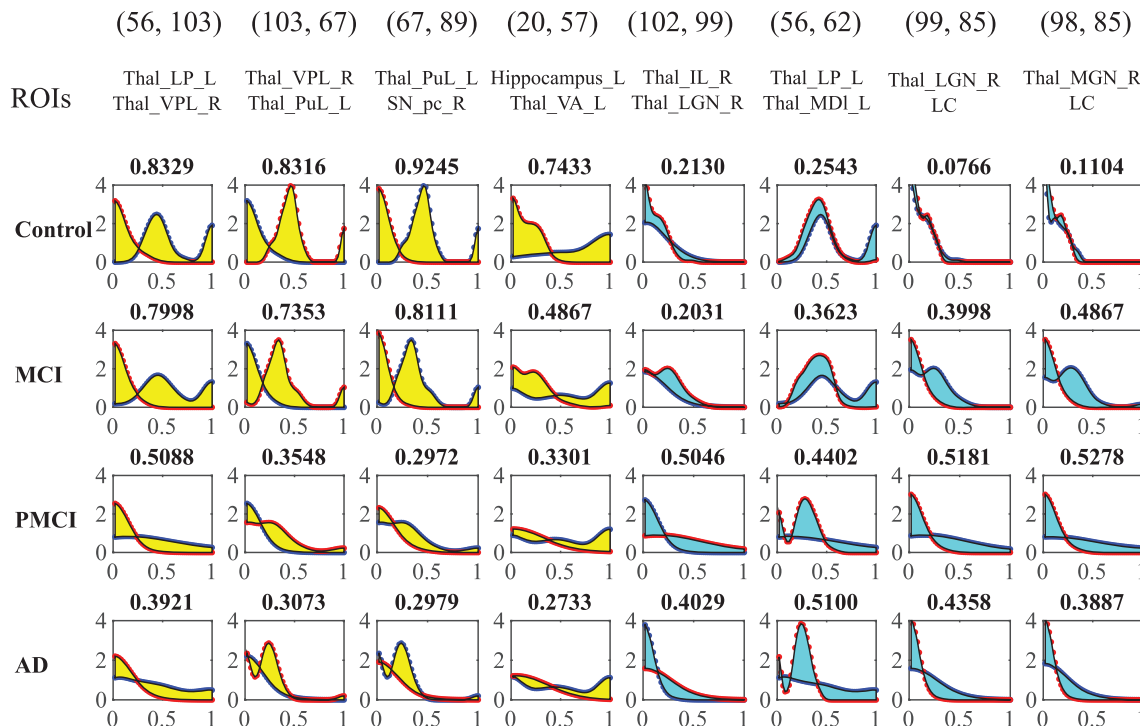
FIGURE 4 Selected pairs of one subject per condition demonstrating negative and positive differences in comparison to control participants; the ROIs, labels, and related node numbers were also included in the figure at the top
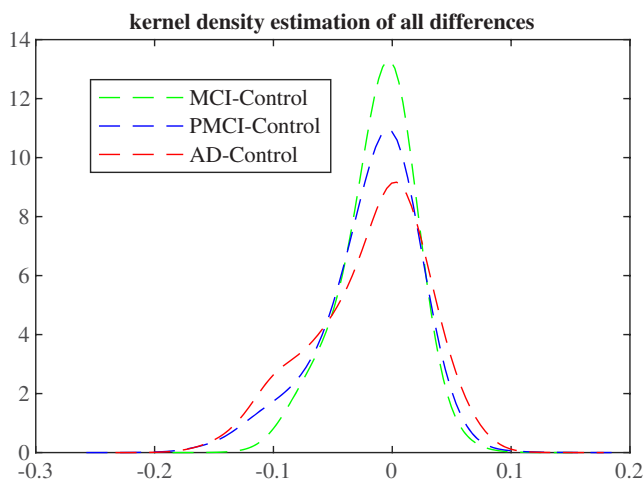

FIGURE 5 Estimation of the kernel density of all differences

depict the condition using its signature network, the GE of DBN formulated with the highest differential pairs is used as the basis. The GCE is then plotted against the number of connections using the process given in Section 2.3. Figure 6 depicts the analysis of GCE vs. the number of connections using positive and negative differences. As a threshold, the "M" values that correspond to the optimal GCE are used.

Considering the negative differences, the thresholds (M) for MCI, PMCI, and AD are 881, 1001, and 1217, respectively. The thresholds determined utilizing positive differences for the conditions MCI,

PMCI, and AD are 492, 587, and 681, respectively. The obtained thresholds are shown in Figure 6 and are the DRNT. Employing the identified DRNT for positive and negative differences forms the brain signatures. Using negative differences, the number of connections required to construct an AD-related signature network is the most, while the number required to form an MCI-related signature network is the smallest. A similar phenomenon is observed when positive differences are used. This demonstrates that as compared to control subjects, the dissimilarities are greatest in AD subjects and lowest in MCI subjects. The next sections discuss the representation of the conditions, their signature networks, and their fusion networks for use in applications.

3.4 | Brain signatures and important ROIs

With threshold levels identified of each condition, the brain signatures obtained utilizing both positive and negative differences are depicted in Figure 7. All connections are binary in nature, and the color representation indicates the node location from 1 to 161. The color representation is solely for the purpose of visualizing the ROI numbers. The signature networks were formed using a proportion of connections between 4% and 10%, and the ROIs containing the largest dissimilarities for each condition are displayed as densely connected nodes. In Figure 7, the left side figures correspond to the brain signatures of MCI, PMCI, and AD associated with the use of negative differences, whereas the right side figures relate to the signature networks associated with MCI, PMCI, and AD associated with the use of positive
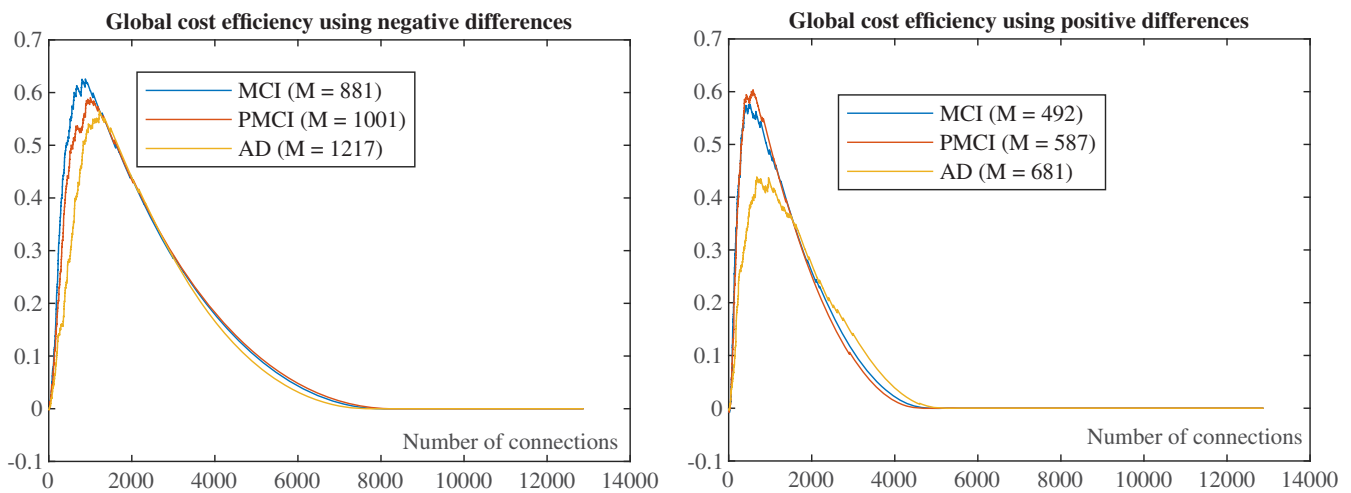
FIGURE 6 Using negative differences to find the disease-related brain network threshold (left) and positive differences to find the disease-related brain network threshold (right)
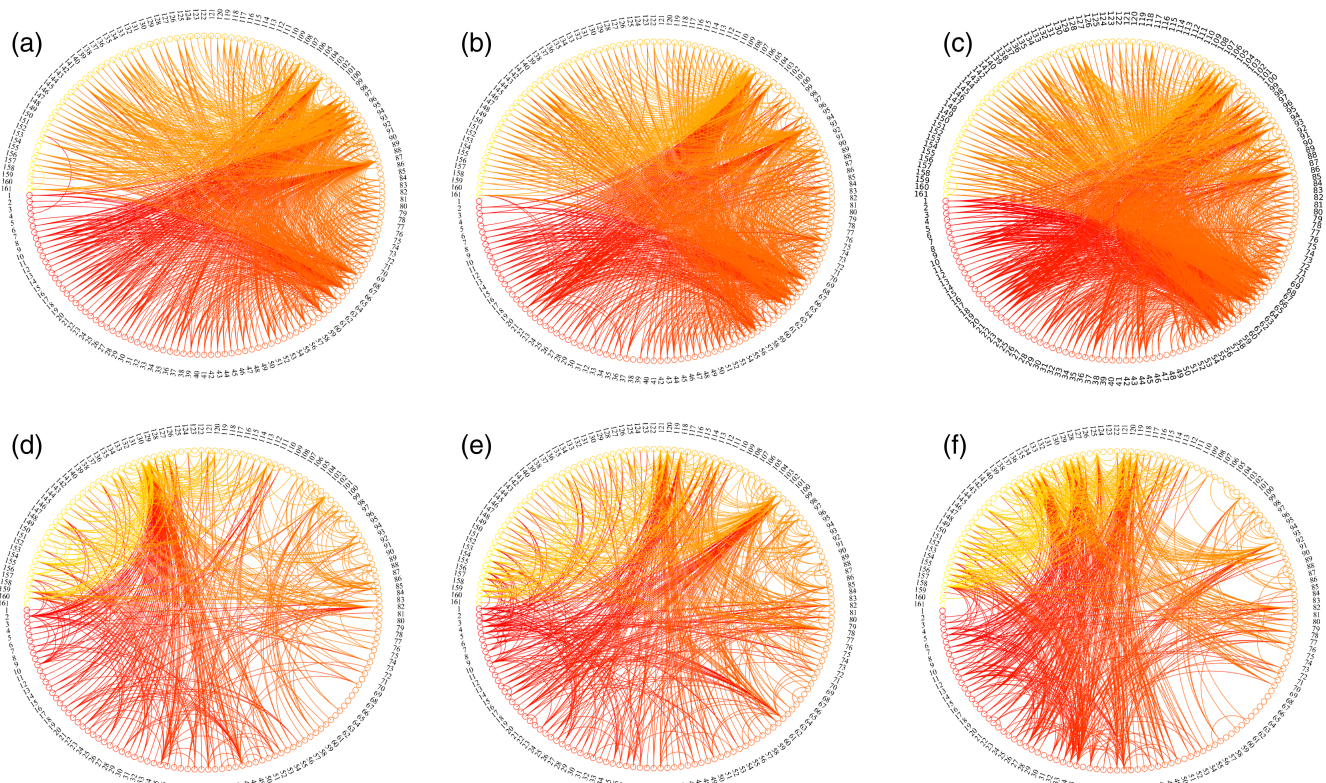

FIGURE 7 Disease-related differential brain networks obtained using the threshold levels identified; (a), (b), and (c) are the networks of MCI, PMCI, and AD of using negative differences; (d), (e), and (f) are the networks of MCI, PMCI, and AD of using positive differences (all connections are binary in nature, and the color representation indicates the node location from 1 [red] to 161 [yellow])

differences. In all scenarios, we see a high degree of interhemispheric connectivity and a low degree of intra-hemispheric connectivity, which is consistent with recent research (Beheshti et al., 2017; Jiang et al., 2017; Kong et al., 2015; Tijms et al., 2012).

Given that the disease often progresses from MCI to PMCI to AD, we identified the common network that exists across conditions in order to comprehend the backbone structure associated with dissimilarities. The fusion of signature networks may be advantageous in a variety of applications (especially to understand the disease progression). As a result, we constructed the fusion networks by combining all the signature networks across conditions. The fusion networks (common network and network of signature networks merged)

constructed utilizing negative and positive differences are depicted in Figure 8. The number of connections in a common network constructed using negative differences is more than the number of connections in a network constructed using positive differences. Also, interhemispheric interactions are prevalent. These patterns may contain information about the course of the disease and may be the key to understand it. As the disease progresses, the brain's disruptions become more severe. To highlight these disruptions in the brain as the disease progresses, the signature networks of MCI, PMCI, and AD with the exclusion of common network are illustrated in Figure 9. The top triangular matrix relates to the signature networks found via the use of negative differences, while the bottom triangular matrix corresponds to the signature networks identified through the use of positive

differences. It is noticed that disruptions spread throughout the brain and that the number of disruptions increases as the disease advances.

Additionally, identifying important ROIs associated with each condition will aid in the understanding of the disease. To find the important regions corresponding to all conditions, the degree of each condition's node is identified. The highest degree nodes (ROIs) are considered significant since they account for a large number of dissimilarities with other ROIs. To find a significant number of significant ROIs, the ROIs are first sorted by degree of presence. Then, the normalized cumulative connections are compared to the ordered arranged ROIs. The ratio of the cumulative connections sum of the selected ROIs to the overall number of connections is used to find the normalized cumulative connections for each condition.

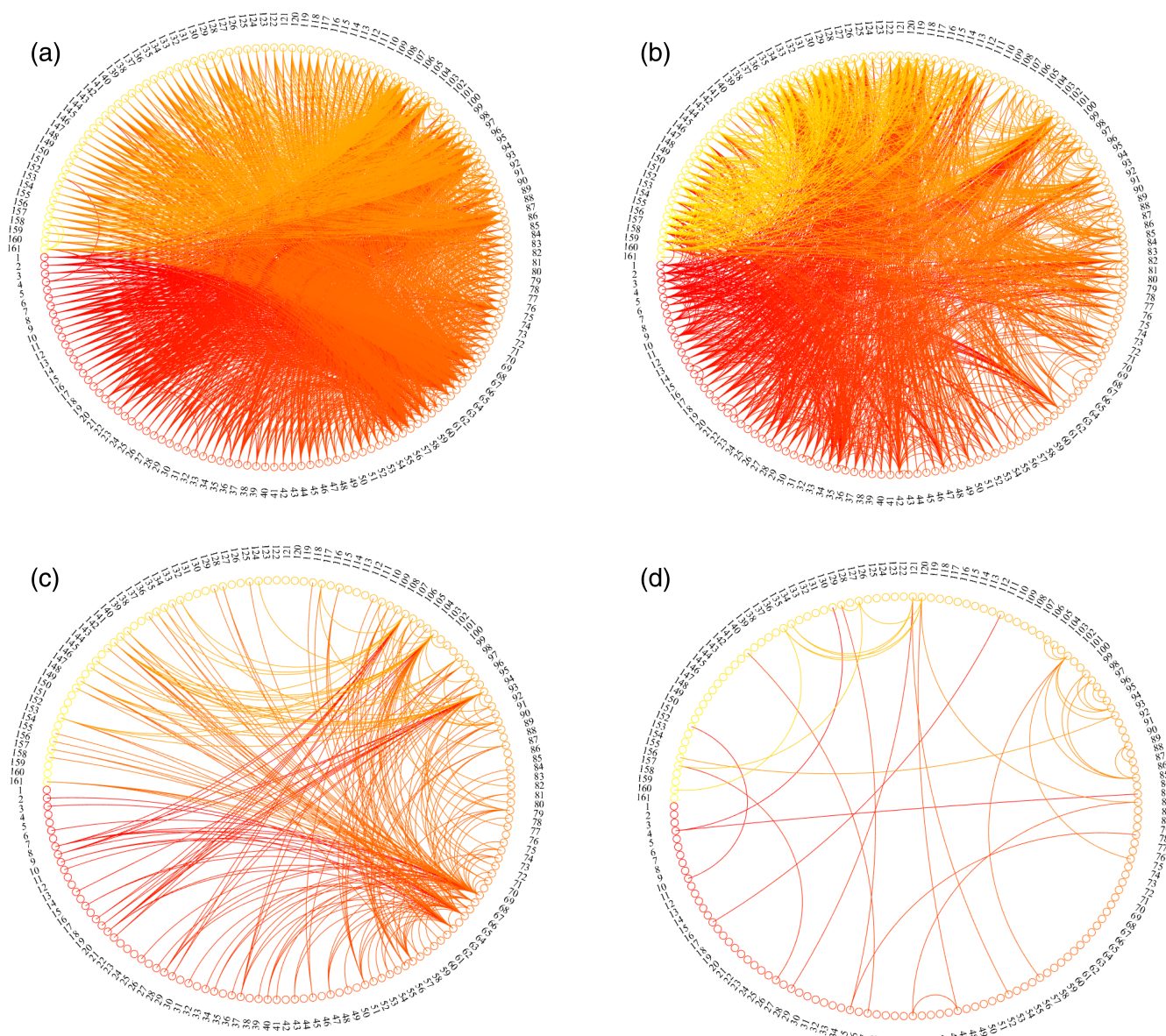**FIGURE 8** Common network patterns and combined network patterns obtained of using the fusion of all conditions; (a) and (b) are the combined networks of using positive and negative differences respectively; (c) and (d) are the common networks of using positive and negative differences respectively (all connections are binary in nature, and the color representation indicates the node location from 1 [red] to 161 [yellow])

Degree Vs orderly arranged ROIs; and normalized cumulative connections Vs orderly arranged ROIs; of all conditions are shown in Figure 10. We can observe that the top few ROIs have a greater degree and are more involved in the condition-specific dissimilarity. Disruptions in these locations may be the cause of the associated disease. The analysis of normalized cumulative connections Vs the ordered ROIs reveals that the top 20 ROIs identified (out of 161) for each condition account for 50% of the dissimilarities (as illustrated in Figure 10, top 20 ROIs account for 50% of total connections). As a result, we identified the top 20 ROIs for each condition as significant ROIs (the network associated with each condition can be seen in 7). Also, these maximum dissimilarity displayed ROIs with other ROIs for each condition is reported in Table. 2. The ROIs identified for all conditions are consistent with those identified in previous research (Koikkalainen et al., 2016; Li et al., 2011; Rimkus et al., 2019; Whitwell, 2009) (ex., ROIs identified correspond to MCI, PMCI, and AD of using negative differences are thalamus and hippocampus; ROIs identified of using positive differences are presented in several ROIs
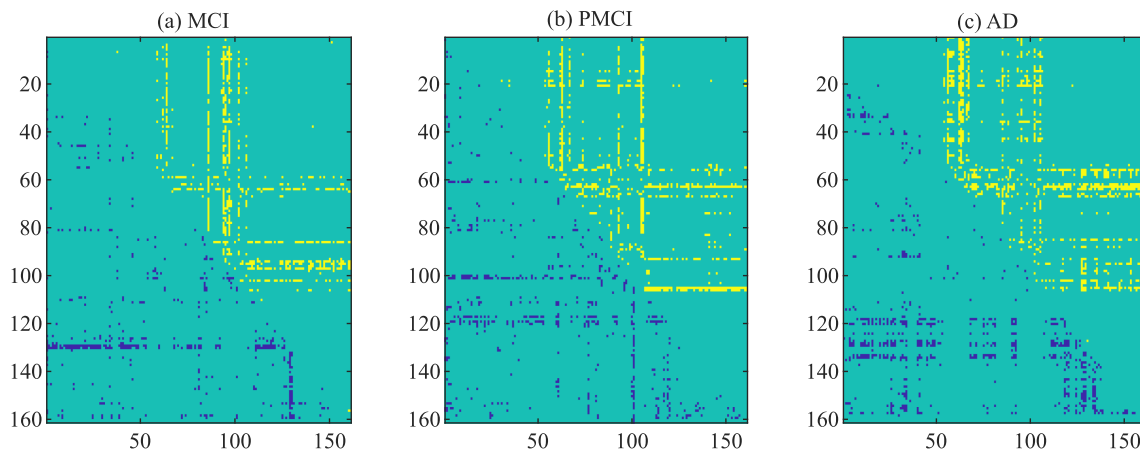
FIGURE 9 Highly disrupted networks with the progression of the disease excluding common network (In the figure, the signature networks of MCI, PMCI, and AD are presented from left to right). All highlighted are binary, with yellow corresponds to negative differences and the blue color corresponds to positive differences
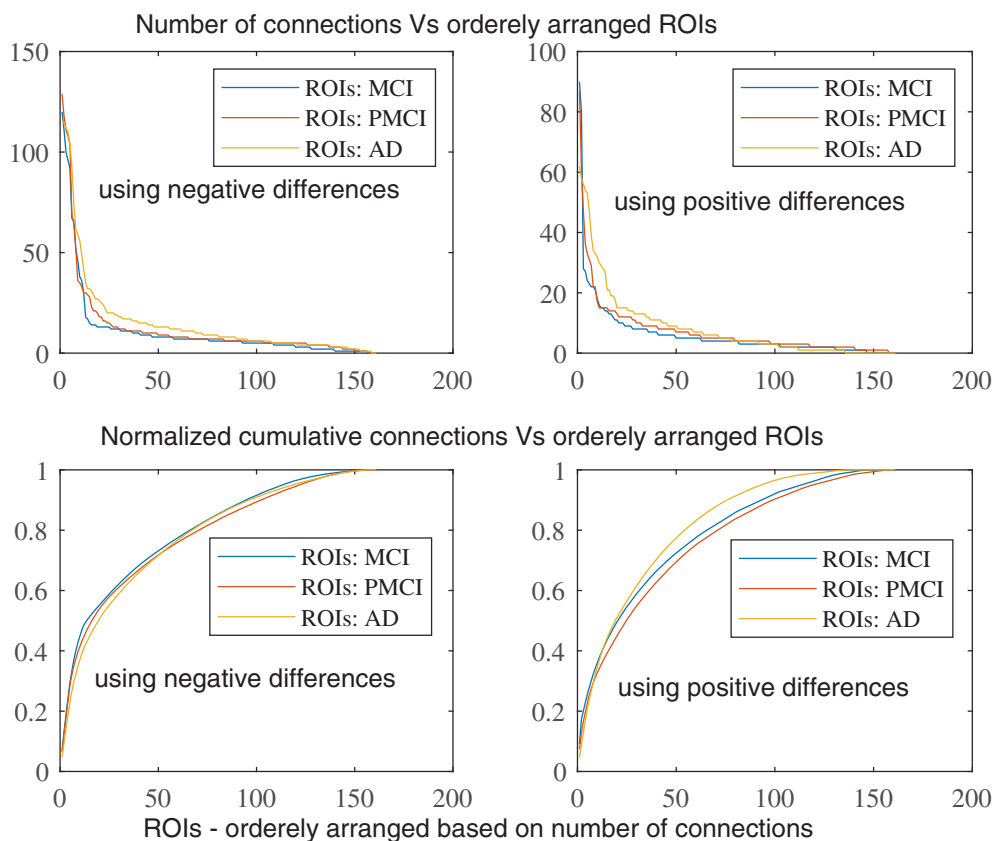

FIGURE 10 ROIs wise connections of brain signatures—for negative differences (left) and positive differences (right)

TABLE 2 ROIs displaying the highest dissimilarities with other ROIs (refer appendix—Table 4 for anatomical descriptions and labeling of all ROIs)

Using negative differences			Using positive differences		
MCI	**PMCI**	**AD**	**MCI**	**PMCI**	**AD**
Thal_PuA_L	Thal_LP_R	Thal_Pul_L	Parietal_Inf_R	Thal_IL_R	Occipital_Mid_R
Red_N_R	Thal_MGN_L	Thal_MGN_L	Parietal_Sup_R	Temporal_Pole_Sup_R	SupraMarginal_R
Thal_MGN_R	Thal_Pul_L	Thal_PuA_L	Precuneus_R	Temporal_Pole_Mid_R	Parietal_Inf_R
Thal_PuL_R	Thal_AV_R	Thal_LGN_L	Thal_IL_R	Thal_MDl_L	Temporal_Sup_R
Thal_VPL_R	Thal_Pul_R	Thal_VA_L	Vermis_9	Temporal_Sup_R	Temporal_Mid_R
Thal_PuM_R	Thal_VA_L	Thal_VPL_R	Cerebelum_Crus2_L	Thal_MDm_R	Occipital_Inf_R
Thal_Pul_L	Thal_LGN_L	Thal_LP_R	Frontal_Sup_2_L	Vermis_4_5	Precuneus_L
Thal_LGN_L	Thal_PuA_L	Raphe	Precuneus_L	Cerebelum_6_R	Caudate_R
Thal_AV_R	Thal_VPL_R	Thal_PuM_R	Frontal_Mid_2_R	Vermis_9	Temporal_Pole_Sup_R
Thal_Pul_R	Red_N_L	Thal_PuL_L	Cerebelum_6_R	LC	Angular_R
Thal_IL_L	Amygdala_L	Thal_Pul_R	Supp_Motor_Area_R	Frontal_Mid_2_R	Temporal_Pole_Sup_L
Thal_PuA_R	Thal_LP_L	Thal_VPL_L	Frontal_Sup_2_R	Frontal_Inf_Orb_2_R	ACC_sub_R
Thal_PuM_L	Thal_Pul_L	Thal_AV_R	LC	Cingulate_Post_L	Frontal_Inf_Oper_R
Thal_LGN_R	Hippocampus_L	Thal_VL_L	Temporal_Pole_Sup_L	Cerebelum_3_R	Angular_L
Hippocampus_R	Vent_Str_R	Thal_IL_L	Raphe	Thal_PuA_R	Occipital_Mid_L
Cerebelum_7b_L	Thal_AV_L	Amygdala_L	Angular_R	Frontal_Mid_2_L	SupraMarginal_L
Vermis_6	Hippocampus_R	SN_pc_R	Temporal_Sup_R	Frontal_Inf_Tri_R	Rolandic_Oper_R
Vent_Str_R	SN_pc_R	Hippocampus_L	Temporal_Pole_Sup_R	Frontal_Sup_Medial_L	Vermis_9
Precentral_R	Cerebelum_7b_L	Thal_LGN_R	Amygdala_L	Cerebelum_4_5_R	Temporal_Sup_L
Olfactory_R	OFClat_L	Caudate_L	Cerebelum_7b_R	Frontal_Inf_Oper_L	Frontal_Inf_Tri_L
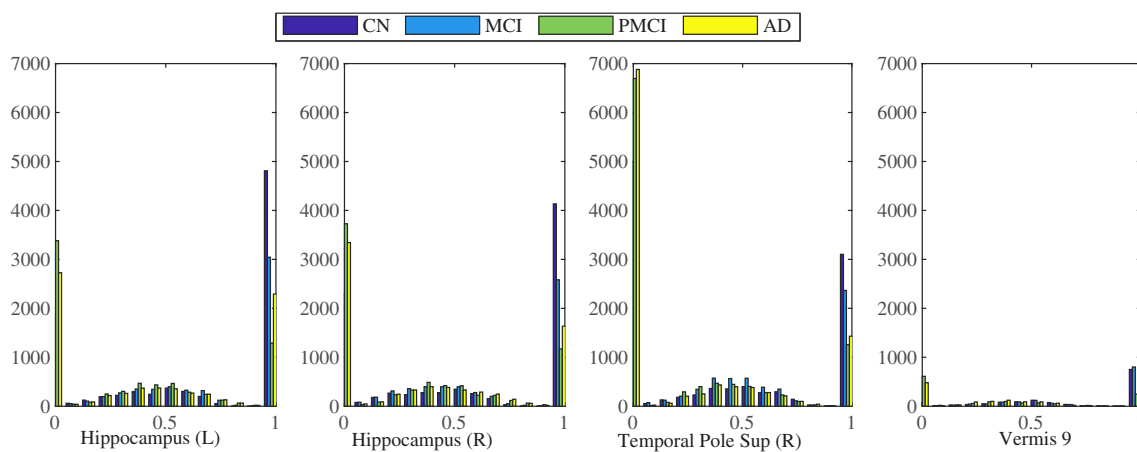
FIGURE 11 Histogram of gray matter TPMs from one subject's identified and selected significant ROIs for each condition. AD, Alzheimer's disease; CN, control subject; MCI, mild cognitive impairment; PMCI, progressive MCI

such as MCI — parietal, frontal, and temporal locations; PMCI—temporal, frontal, and AD—temporal, frontal, and occipital). To show the disruption of the identified important ROIs, one individual per condition of the selected ROIs from the identified ROIs and their gray matter TPMs histogram is demonstrated in Figure 11. In the ROIs designated as significant ROIs, we can observe the disruption of the gray matter TPM as the disease advances. Overall, the shown network analysis of brain signatures demonstrates that the proposed methodologies may bring various new insights into disease understanding, and these

signature networks may be useful for clinical analysis and a variety of other network-based applications.

3.5 | Application

To demonstrate the use of signature networks in applications and to evaluate the identified brain signatures, the 200 examination subjects (50 each of control, MCI, PMCI, and AD) at the time of diagnosis are
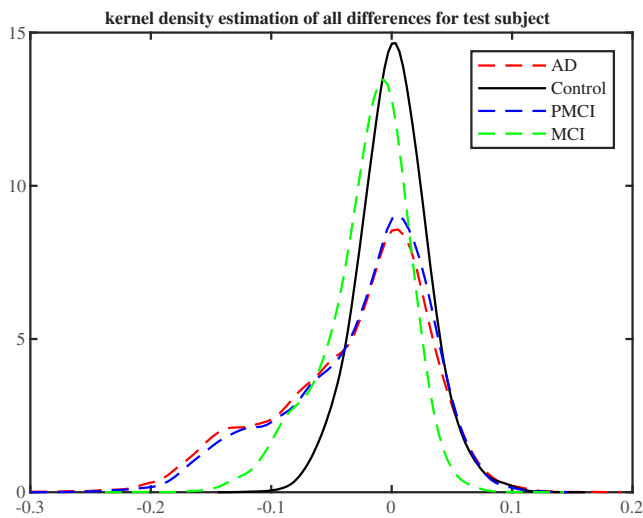
FIGURE 12 Kernel density estimation of all differences for examination subjects (to find the difference values, the control group of reference subjects is used)
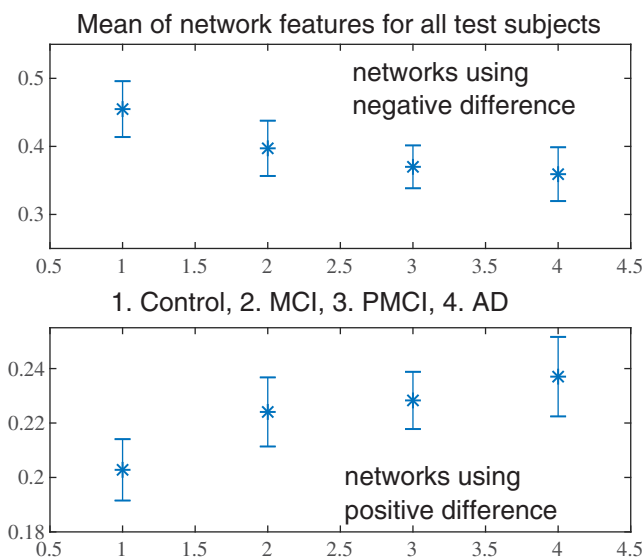

FIGURE 13 Mean of network features for examination subjects of all conditions—error bar shows the standard deviation

considered for classification using the brain signatures identified in this study. The identical ROIs created for reference subjects are used to form the brain networks associated with examination subjects (also, the excluded voxel locations are the same as described for reference subjects). To visualize the differences, the kernel density estimation of all the differences for all examination subjects is shown in Figure 12. The reference data's control individuals are used to determine the differences. The differences displayed in Figure 12 of all conditions displayed similar observations made for reference subjects. PMCI and AD, in comparison to MCI, have a greater range of differences. The signature networks identified through the use of data from reference subjects are then used to form the features of examination subjects'

TABLE 3 Classification of MCI, PMCI, and AD (reference subjects are excluded from the classification analysis as they were utilized solely to generate the brain signatures)

	Control vs. MCI	Control vs. PMCI	MCI vs. PMCI	Control vs. AD	All (4 classes)
Accuracy (%)	83.7	85.3	83.9	85.3	78.4

data. The fusion network, or the pattern of all the brain signatures combined, is used to classify subjects as control, MCI, PMCI, or AD.

Prior to obtaining the classification results for examination subjects, we would like to show the behavior of all examination subjects in order to highlight how the identified brain signatures are relevant for classification. To do this, the mean of Sorensen distance dissimilarity of the brain signature networks of all subjects and all conditions for examination subjects is determined and presented in Figure 13. The standard deviation identified of mean networks for all subjects is also depicted in the figure as an error bar. As illustrated in the figure, there are significant differences in the average signature networks. This difference level may be critical in discriminating the subject. Thus, the identified brain signatures can be used for classification and are selected as an example to demonstrate the use of brain signatures.

For evaluation purposes, the combined network's (fusion network obtained of using reference subjects) Sorensen distance dissimilarities as features of each examination subject were considered for classification into control, MCI, PMCI, and AD. Due to the fact that the reference subjects were utilized solely to generate the brain signatures, 2/3 of the examination subjects are chosen for training and the remaining 1/3 for testing. PCA is used to retain enough components to account for 95% of the variation. Classification of a) Control vs. MCI b) Control vs. PMCI c) MCI vs. PMCI d) control vs. AD and e) All four classes (Control, MCI, PMCI, and AD) is accomplished using SVMs with threefold cross-validation and a one-against-one strategy. The classification accuracies obtained by employing Sorensen distance dissimilarities as features in fusion networks (combined network of all the brain signatures) are summarized in Table 3. Classification accuracy of 78.4% (4 classes) was obtained when subjects were classified as control, MCI, PMCI, or AD. And an average of 84.7% (2 classes) accuracy in identifying individuals as control vs. (MCI, PMCI, AD). Classification accuracy of 83.9% for MCI vs. PMCI highlights the early identification of PMCI using the proposed approach. The results indicate that the brain signatures identified can be employed in applications.

4 | DISCUSSION AND CONCLUSIONS

Previously, gray matter and white matter tracts were used to study structural network changes associated with a variety of illnesses. The majority of research had trouble investigating an individual because these networks were constructed utilizing correlations between

TABLE 4 Anatomical description and labels of all nodes (LH—Left hemisphere and RH—Right hemisphere)

Anatomical description	Label		Node number	
	LH	RH	LH	RH
Precentral gyrus	Precentral_L	Precentral_R	1	161
Superior frontal gyrus, dorsolateral	Frontal_Sup_2_L	Frontal_Sup_2_R	2	160
Middle frontal gyrus	Frontal_Mid_2_L	Frontal_Mid_2_R	3	159
Inferior frontal gyrus, opercular part	Frontal_Inf_Oper_L	Frontal_Inf_Oper_R	4	158
Inferior frontal gyrus, triangular part	Frontal_Inf_Tri_L	Frontal_Inf_Tri_R	5	157
IFG pars orbitalis	Frontal_Inf_Orb_2_L	Frontal_Inf_Orb_2_R	6	156
Rolandic operculum	Rolandic_Oper_L	Rolandic_Oper_R	7	155
Supplementary motor area	Supp_Motor_Area_L	Supp_Motor_Area_R	8	154
Olfactory cortex	Olfactory_L	Olfactory_R	9	153
Superior frontal gyrus, medial	Frontal_Sup_Medial_L	Frontal_Sup_Medial_R	10	152
Superior frontal gyrus, medial orbital	Frontal_Med_Orb_L	Frontal_Med_Orb_R	11	151
Gyrus rectus	Rectus_L	Rectus_R	12	150
Medial orbital gyrus	OFCmed_L	OFCmed_R	13	149
Anterior orbital gyrus	OFCant_L	OFCant_R	14	148
Posterior orbital gyrus	OFCpost_L	OFCpost_R	15	147
Lateral orbital gyrus	OFClat_L	OFClat_R	16	146
Insula	Insula_L	Insula_R	17	145
Middle cingulate & paracingulate gyri	Cingulate_Mid_L	Cingulate_Mid_R	18	144
Posterior cingulate gyrus	Cingulate_Post_L	Cingulate_Post_R	19	143
Hippocampus	Hippocampus_L	Hippocampus_R	20	142
Parahippocampal gyrus	ParaHippocampal_L	ParaHippocampal_R	21	141
Amygdala	Amygdala_L	Amygdala_R	22	140
Calcarine fissure and surrounding cortex	Calcarine_L	Calcarine_R	23	139
Cuneus	Cuneus_L	Cuneus_R	24	138
Lingual gyrus	Lingual_L	Lingual_R	25	137
Superior occipital gyrus	Occipital_Sup_L	Occipital_Sup_R	26	136
Middle occipital gyrus	Occipital_Mid_L	Occipital_Mid_R	27	135
Inferior occipital gyrus	Occipital_Inf_L	Occipital_Inf_R	28	134
Fusiform gyrus	Fusiform_L	Fusiform_R	29	133
Postcentral gyrus	Postcentral_L	Postcentral_R	30	132
Superior parietal gyrus inferior parietal gyrus, excluding	Parietal_Sup_L	Parietal_Sup_R	31	131
Supramarginal and angular gyri	Parietal_Inf_L	Parietal_Inf_R	32	130
SupraMarginal gyrus	SupraMarginal_L	SupraMarginal_R	33	129
Angular gyrus	Angular_L	Angular_R	34	128
Precuneus	Precuneus_L	Precuneus_R	35	127
Paracentral lobule	Paracentral_Lobule_L	Paracentral_Lobule_R	36	126
Caudate nucleus	Caudate_L	Caudate_R	37	125
Lenticular nucleus, putamen	Putamen_L	Putamen_R	38	124
Lenticular nucleus, pallidum	Pallidum_L	Pallidum_R	39	123
Heschl's gyrus	Heschl_L	Heschl_R	40	122
Superior temporal gyrus	Temporal_Sup_L	Temporal_Sup_R	41	121
Temporal pole: Superior temporal gyrus	Temporal_Pole_Sup_L	Temporal_Pole_Sup_R	42	120
Middle temporal gyrus	Temporal_Mid_L	Temporal_Mid_R	43	119
Temporal pole: Middle temporal gyrus	Temporal_Pole_Mid_L	Temporal_Pole_Mid_R	44	118
Inferior temporal gyrus	Temporal_Inf_L	Temporal_Inf_R	45	117

TABLE 4 (Continued)

Anatomical description	Label		Node number	
	LH	RH	LH	RH
Crus I of cerebellar hemisphere	Cerebelum_Crus1_L	Cerebelum_Crus1_R	46	116
Crus II of cerebellar hemisphere	Cerebelum_Crus2_L	Cerebelum_Crus2_R	47	115
Lobule III of cerebellar hemisphere	Cerebelum_3_L	Cerebelum_3_R	48	114
Lobule IV, V of cerebellar hemisphere	Cerebelum_4_5_L	Cerebelum_4_5_R	49	113
Lobule VI of cerebellar hemisphere	Cerebelum_6_L	Cerebelum_6_R	50	112
Lobule VIIB of cerebellar hemisphere	Cerebelum_7b_L	Cerebelum_7b_R	51	111
Lobule VIII of cerebellar hemisphere	Cerebelum_8_L	Cerebelum_8_R	52	110
Lobule IX of cerebellar hemisphere	Cerebelum_9_L	Cerebelum_9_R	53	109
Lobule X of cerebellar hemisphere	Cerebelum_10_L	Cerebellum_10_R	54	108
Thalamus, Anteroventral nucleus	Thal_AV_L	Thal_AV_R	55	107
Lateral posterior	Thal_LP_L	Thal_LP_R	56	106
Ventral anterior	Thal_VA_L	Thal_VA_R	57	105
Ventral lateral	Thal_VL_L	Thal_VL_R	58	104
Ventral posterolateral	Thal_VPL_L	Thal_VPL_R	59	103
Intralaminar	Thal_IL_L	Thal_IL_R	60	102
Mediodorsal medial magnocellular	Thal_MDm_L	Thal_MDm_R	61	101
Mediodorsal lateral parvocellular	Thal_MDl_L	Thal_MDl_R	62	100
Lateral geniculate	Thal_LGN_L	Thal_LGN_R	63	99
Medial geniculate	Thal_MGN_L	Thal_MGN_R	64	98
Pulvinar anterior	Thal_PuA_L	Thal_PuA_R	65	97
Pulvinar medial	Thal_PuM_L	Thal_PuM_R	66	96
Pulvinar lateral	Thal_PuL_L	Thal_PuL_R	67	95
Pulvinar inferior	Thal_PuI_L	Thal_PuI_R	68	94
Anterior cingulate cortex, subgenual	ACC_sub_L	ACC_sub_R	69	93
Anterior cingulate cortex, pregenual	ACC_pre_L	ACC_pre_R	70	92
Anterior cingulate cortex, supracallosal	ACC_sup_L	ACC_sup_R	71	91
Ventral striatum	Vent_Str_L	Vent_Str_R	72	90
Substantia nigra, pars compacta	SN_pc_L	SN_pc_R	73	89
Substantia nigra, pars reticulata	SN_pr_L	SN_pr_R	74	88
Red nucleus	Red_N_L	Red_N_R	75	87
Lobule I, II of vermis	Vermis_1_2		76	
Lobule III of vermis	Vermis_3		77	
Lobule IV, V of vermis	Vermis_4_5		78	
Lobule VI of vermis	Vermis_6		79	
Lobule VII of vermis	Vermis_7		80	
Lobule VIII of vermis	Vermis_8		81	
Lobule IX of vermis	Vermis_9		82	
Lobule X of vermis	Vermis_10		83	
Ventral tegmental area	VTA		84	
Locus coeruleus	LC		85	
Raphe nucleus, dorsal and median	Raphe		86	

averaged ROIs of thickness or volume from multiple subjects. We provided a framework for deriving an individual network from sMRI and methods for identifying the brain signatures and significant ROIs in this work. The proposed methods were successful in identifying individual networks based on sMRI data and in forming brain signature networks and significant ROIs associated with any condition. These

findings indicate that analyzing an individual's defined signature networks may provide critical information for recognizing brain abnormalities. Additionally, by analyzing these brain signatures using graph theory, one can examine the brain from a network neuroscientific perspective.

To form the connectivity, we utilized the Sorensen distance between the TPMs distributions of the defined ROIs. Numerous other techniques, such as those discussed in (Cha, 2007), can be used to determine the weights of edges. All of these measurements are indirect indicators of connectivity representation, and identifying brain signatures associated with these methods could serve as a complement to anatomical connectivity. The Sorensen distance metric is chosen because it is simpler and avoids division by zeros. The proposed approach for generating brain signatures is based on differential networks, and the thresholds are determined based on the importance of those differences in terms of global efficiency. The threshold selection method can be used to depict any brain activity with optimal connections. The integrated networks of all the conditions can be utilized to discriminate between many diseases or a disease at different time points (the study of the network changes at several time points could help understand the disease progression). The proposed methodologies also enable us to better comprehend illness progression (an increase of dissimilarities observed with the disease progression for both reference subjects and examination subjects), and the addition of patterns at various time points may enable us to gain a better understanding of the condition.

In this paper, we considered the fusion network as simple shared patterns (common networks) or integrated (combined) networks of all the conditions identified. Further observation of signature networks (as in Figure7) reveals that the common patterns have only a few connections (as depicted in Figure 8). This illustrates how distinctive each condition is. The same can be also observed in the ROIs identified of each condition (shown in Table 2, they have several distinctive ROIs due to the distinctive nature of the signature networks). This helps us to understand the analysis of the identified significant networks through their individual contributions (ex. classified MCI vs. PMCI with an accuracy of 83.9% as they have distinctive patterns; classification of control vs. PMCI and control vs. AD indicate that the identification of PMCI and AD is comparatively easy as they display distinctive nature in their signature networks).

Fusion networks can be also obtained by forming the specificity loss that balances the contribution and commonality loss that considers the similarity of each selected network. The combination of fusion network (contains the rich information of all the selected conditions) and graph convolution network improves disease classification accuracy while also providing insight into the underlying connectivity in the brain. Fusion networks involving multiple conditions or diseases may be difficult to implement. So, optimal fusion network formation with graph fusion network algorithms for disease quantification will be considered in future analysis. There is a lot of potential in using common patterns as disease markers which could be challenging as well.

Several significant ROIs associated with MCI, PMCI, and AD were identified in this study. It was observed that the ROIs found using

negative differences corresponded to regions of the brain that are critical for information processing. Positive differences identified ROIs associated with memory, attention, and a variety of functional and learning capacities. These findings demonstrate that abnormalities in the brain were particularly severe in disease-related regions, and the identified regions and patterns can be employed in a variety of applications (ex. the constructed brain signatures can be used as a basis in the analysis of extracting deep features from sMRI using graph convolution approach). Comparable classification accuracy with the identified brain signature networks demonstrates the suggested methodology's promise in the fields of brain mapping, brain communication, and any other application involving brain networks. The proposed approaches were validated using sMRI data from controls, MCI, PMCI, and AD subjects. Additionally, the framework can be used to research a variety of other neurological and mental disorders. The future investigation will also focus on the individual network changes associated with illness development utilizing graph metrics. Only 260 subjects were considered in this study (60 for forming the brain signatures and 200 for the evaluation procedure), as the primary objective of this work is to build a framework for recognizing brain signatures using sMRI. Future research will include a greater number of subjects and will focus on improving the accuracy as well. Overall, the proposed methodologies may contribute unique insights to our understanding of the brain's basic structures, and we expect that this contribution will be of interest to the neuroscientific community.

CONFLICT OF INTERESTS

No conflict of interest was declared.

DATA AVAILABILITY STATEMENT

Data sharing is not applicable to this article as no new data were created or analyzed in this study.

ORCID

Venkateswarlu Gonuguntla https://orcid.org/0000-0002-6857-2254

REFERENCES

Apostolova, L. G., & Thompson, P. M. (2007). Brain mapping as a tool to study neurodegeneration. *Neurotherapeutics*, 4(3), 387–400.

B, F. (2012). FreeSurfer. *NeuroImage*, 62(2), 774–781.

Bassett, D. S., Bullmore, E., Verchinski, B. A., Mattay, V. S., Weinberger, D. R., & Meyer-Lindenberg, A. (2008). Hierarchical organization of human cortical networks in health and schizophrenia. *Journal of Neuroscience*, 28(37), 9239–9248.

Beheshti, I., Maikusa, N., Daneshmand, M., Matsuda, H., Demirel, H., & Anbarjafari, G. (2017). Classification of Alzheimer's disease and prediction of mild cognitive impairment conversion using histogram-based analysis of patient-specific anatomical brain connectivity networks. *Journal of Alzheimer's Disease*, 60(1), 295–304.

Brier, M. R., Thomas, J. B., & Ances, B. M. (2014). Network dysfunction in Alzheimer's disease: Refining the disconnection hypothesis. *Brain Connectivity*, 4(5), 299–311.

Bullmore, E., & Sporns, O. (2009). Complex brain networks: Graph theoretical analysis of structural and functional systems. *Nature Reviews Neuroscience*, 10(3), 186–198.

Cha, S. H. (2007). Comprehensive survey on distance/similarity measures between probability density functions. *City*, 1(2), 1.

Chen, Z. J., He, Y., Rosa-Neto, P., Germann, J., & Evans, A. C. (2008). Revealing modular architecture of human brain structural networks by using cortical thickness from MRI. *Cerebral Cortex*, 18(10), 2374–2381.

Collins, D. L., Holmes, C. J., Peters, T. M., & Evans, A. C. (1995). Automatic 3-D model-based neuroanatomical segmentation. *Human Brain Mapping*, 3(3), 190–208.

Dai, Z., Lin, Q., Li, T., Wang, X., Yuan, H., Yu, X., … Wang, H. (2019). Disrupted structural and functional brain networks in Alzheimer's disease. *Neurobiology of Aging*, 75, 71–82.

Dimitriadis, S. I., Salis, C., Tarnanas, I., & Linden, D. E. (2017). Topological filtering of dynamic functional brain networks unfolds informative chronnectomics: A novel data-driven thresholding scheme based on orthogonal minimal spanning trees (OMSTs). *Frontiers in Neuroinformatics*, 11, 28.

Filippi, M., & Agosta, F. (2011). Structural and functional network connectivity breakdown in Alzheimer's disease studied with magnetic resonance imaging techniques. *Journal of Alzheimer's Disease*, 24(3), 455–474.

Filippi, M., Basaia, S., Canu, E., Imperiale, F., Magnani, G., Falautano, M., … Agosta, F. (2020). Changes in functional and structural brain connectome along the Alzheimer's disease continuum. *Molecular Psychiatry*, 25(1), 230–239.

Frisoni, G. B., Fox, N. C., Jack, C. R., Scheltens, P., & Thompson, P. M. (2010). The clinical use of structural MRI in Alzheimer disease. *Nature Reviews Neurology*, 6(2), 67–77.

Gong, G., He, Y., Concha, L., Lebel, C., Gross, D. W., Evans, A. C., & Beaulieu, C. (2009). Mapping anatomical connectivity patterns of human cerebral cortex using in vivo diffusion tensor imaging tractography. *Cerebral Cortex*, 19(3), 524–536.

Gonuguntla V, Kim JH. EEG-Based Functional Connectivity Representation using Phase Locking Value for Brain Network Based Applications. In: 2020 42nd Annual International Conference of the IEEE Engineering in Medicine & Biology Society (EMBC) IEEE; 2020. p. 2853–2856

Gonuguntla, V., Veluvolu, K. C., & Kim, J. H. (2020). Recognition of event-associated brain functional networks in EEG for brain network based applications. In *2020 IEEE 17th International Symposium on Biomedical Imaging* (pp. 271–274). IEEE.

He, Y., Chen, Z. J., & Evans, A. C. (2007). Small-world anatomical networks in the human brain revealed by cortical thickness from MRI. *Cerebral Cortex*, 17(10), 2407–2419.

Hojjati, S. H., Ebrahimzadeh, A., Khazaee, A., Babajani-Feremi, A., & Alzheimer's Disease Neuroimaging Initiative. (2018). Predicting conversion from MCI to AD by integrating rs-fMRI and structural MRI. *Computers in Biology and Medicine*, 102, 30–39.

Jenkinson, M., Beckmann, C. F., Behrens, T. E. J., Woolrich, M. W., & Smith, S. M. (2012). Fsl. *NeuroImage*, 62, 782–790.

Jiang, J., Zhou, H., Duan, H., Liu, X., Zuo, C., Huang, Z., … Alzheimer's Disease Neuroimaging Initiative. (2017). A novel individual-level morphological brain networks constructing method and its evaluation in PET and MR images. *Heliyon*, 3(12), e00475.

Khundrakpam, B. S., Reid, A., Brauer, J., Carbonell, F., Lewis, J., Ameis, S., … O'Neill, J. (2013). Developmental changes in organization of structural brain networks. *Cerebral Cortex*, 23(9), 2072–2085.

Koikkalainen, J., Rhodius-Meester, H., Tolonen, A., Barkhof, F., Tijms, B., Lemstra, A. W., … Lötjönen, J. (2016). Differential diagnosis of neurodegenerative diseases using structural MRI data. *NeuroImage: Clinical*, 11, 435–449.

Kong XZ, Liu Z, Huang L, Wang X, Yang Z, Zhou G, et al. Mapping individual brain networks using statistical similarity in regional morphology from MRI. *PloS One* 2015;10(11):e0141840.

Li, K., Luo, X., Zeng, Q., Huang, P., Shen, Z., Xu, X., … Alzheimer's Disease Neuroimaging Initiative. (2019). Gray matter structural covariance networks changes along the Alzheimer's disease continuum. *NeuroImage: Clinical*, 23, 101828.

Li, X., Coyle, D., Maguire, L., Watson, D. R., & McGinnity, T. M. (2011). Gray matter concentration and effective connectivity changes in

Alzheimer's disease: A longitudinal structural MRI study. *Neuroradiology*, 53(10), 733–748.

Mazziotta, J., Toga, A., Evans, A., Fox, P., Lancaster, J., Zilles, K., … Mazoyer, B. (2001). A probabilistic atlas and reference system for the human brain: International consortium for brain mapping (ICBM). *Philosophical Transactions of the Royal Society of London Series B: Biological Sciences*, 356(1412), 1293–1322.

McCune, B., Grace, J. B., & Urban, D. L. (2002). *Analysis of ecological communities*. Gleneden Beach, Oregon: MjM software design.

Pastore, M., & Calcagnì, A. (2019). Measuring distribution similarities between samples: A distribution-free overlapping index. *Frontiers in Psychology*, 10, 1089.

Rimkus, C. M., Schoonheim, M. M., Steenwijk, M. D., Vrenken, H., Eijlers, A. J., Killestein, J., … Tijms, B. M. (2019). Gray matter networks and cognitive impairment in multiple sclerosis. *Multiple Sclerosis Journal*, 25(3), 382–391.

Rolls, E. T., Huang, C. C., Lin, C. P., Feng, J., & Joliot, M. (2020). Automated anatomical labelling atlas 3. *NeuroImage*, 206, 116189.

Rubinov, M., & Sporns, O. (2010). Complex network measures of brain connectivity: Uses and interpretations. *NeuroImage*, 52(3), 1059–1069.

Salvatore, C., Cerasa, A., & Castiglioni, I. (2018). MRI characterizes the progressive course of AD and predicts conversion to Alzheimer's dementia 24 months before probable diagnosis. *Frontiers in Aging Neuroscience*, 10, 135.

Sanz-Arigita, E. J., Schoonheim, M. M., Damoiseaux, J. S., Rombouts, S. A., Maris, E., Barkhof, F., … Stam, C. J. (2010). Loss of 'small-world' networks in Alzheimer's disease: Graph analysis of FMRI resting-state functional connectivity. *PLoS One*, 5(11), e13788.

Smith, S. M., Jenkinson, M., Woolrich, M. W., Beckmann, C. F., Behrens, T. E., Johansen-Berg, H., … Matthews, P. M. (2004). Advances in functional and structural MR image analysis and implementation as FSL. *Neuroimage*, 23, S208–S219.

Sorensen, T. (1948). A method of establishing groups of equal amplitude in plant sociology based on similarity of species and its application to analyses of the vegetation on Danish commons. *Biologiske Skrifter/Kongelige Danske Videnskabernes Selskab*, 5(4), 1–34 NS Kuzminova 2008; p. 2008–2012.

Sporns, O. (2013). Structure and function of complex brain networks. *Dialogues in Clinical Neuroscience*, 15(3), 247–262.

Spulber, G., Simmons, A., Muehlboeck, J. S., Mecocci, P., Vellas, B., Tsolaki, M., … for the AddNeuroMed consortium and for the Alzheimer Disease Neuroimaging Initiative. (2013). An MRI-based index to measure the severity of Alzheimer's disease-like structural pattern in subjects with mild cognitive impairment. *Journal of Internal Medicine*, 273(4), 396–409.

Tijms, B. M., Seriès, P., Willshaw, D. J., & Lawrie, S. M. (2012). Similarity-based extraction of individual networks from gray matter MRI scans. *Cerebral Cortex*, 22(7), 1530–1541.

Vemuri, P., & Jack, C. R. (2010). Role of structural MRI in Alzheimer's disease. *Alzheimer's Research & Therapy*, 2(4), 23.

Whitwell, J. L. (2009). Voxel-based morphometry: An automated technique for assessing structural changes in the brain. *Journal of Neuroscience*, 29(31), 9661–9664.

Woolrich, M. W., Jbabdi, S., Patenaude, B., Chappell, M., Makni, S., Behrens, T., … Smith, S. M. (2009). Bayesian analysis of neuroimaging data in FSL. *NeuroImage*, 45(1), S173–S186.